

Response of Non-premixed Jet Flames to Blast Waves

Akhil Aravind¹, Gautham Vadlamudi¹, and Saptarshi Basu^{1,2*}

*: Corresponding author email: sbasu@iisc.ac.in

Affiliations:

¹ Department of Mechanical Engineering, Indian Institute of Science, Bangalore 560012, India

² Interdisciplinary Centre for Energy Research (ICER), Indian Institute of Science, Bangalore 560012, India

S1. Otsu Thresholding Algorithm

This section provides an overview of Otsu's thresholding technique¹ employed in the current study to binarize flame images, facilitating subsequent post-processing and analysis.

Step-1: Histogram Calculation and Probability Distribution

Compute the histogram of the image, which represents the frequency of each intensity level in the image. Then, calculate the probabilities of each intensity level, $p(i)$, by normalizing the histogram.

In the current experiments, the images from the high-speed camera were converted into 8-bit grayscale images prior to post-processing. Hence, the intensity levels varied from 0 to 255, and correspondingly, the total number of intensity levels (L) is 255

Step-2: Class Statistics Estimation

Define a threshold value (t^*) and then categorise the image into two classes - Class-1 (C_1) wherein the pixel intensities are less than or equal to the threshold, and Class-2 (C_2) for which the pixel intensities are greater than t^* . The probabilities of each class can then be estimated as,

$$w_1(t^*) = \sum_0^{t^*} p(i) \quad w_2(t^*) = \sum_{(t^*+1)}^{(L-1)} p(i) \quad (1)$$

Likewise, the mean intensity of each class can be estimated as,

$$\mu_1(t^*) = \frac{\sum_0^{t^*} i p(i)}{w_1(t^*)} \quad \mu_2(t^*) = \frac{\sum_{(t^*+1)}^{(L-1)} i p(i)}{w_2(t^*)} \quad (2)$$

We can now define the variance within each class as,

$$\sigma_1^2(t^*) = \frac{\sum_0^{t^*} (i - \mu_1(t^*))^2 p(i)}{w_1(t^*)} \quad \sigma_2^2(t^*) = \frac{\sum_{(t^*+1)}^{(L-1)} (i - \mu_2(t^*))^2 p(i)}{w_2(t^*)} \quad (3)$$

The weighted sum of these intra-class variances (σ_W^2) can be defined as,

$$\sigma_W^2(t^*) = w_1(t^*)\sigma_1^2(t^*) + w_2(t^*)\sigma_2^2(t^*) \quad (4)$$

The inter-class variance ($\sigma_B^2(t^*)$) measures how distinct or separable the two classes (C_1 and C_2) are for a given threshold t^* . It quantifies the variance due to the difference between the mean intensity values of the two classes.

$$\sigma_B^2(t^*) = w_1(t^*)w_2(t^*)[\mu_1(t^*) - \mu_2(t^*)]^2 \quad (5)$$

It should be noted that t^* can assume any value between 0 and 255 for the 8-bit grayscale images used in the current study. Thus, the above-mentioned statistical parameters can be estimated for all the values of t^* ranging from 0 to 255.

Step-3: Estimation of Optimal Threshold

The value of t^* that maximises the inter-class variance is the optimal threshold value (t_{opt}^*)

Step-4: Binarization of the Image based on the optimal threshold value

t_{opt}^* is used to separate the image into two classes: Foreground and Background. Pixels with intensities greater than t_{opt}^* are assigned as foreground, and pixels with intensity lesser than or equal to $\leq t_{opt}^*$ are assigned as background.

S2. Bach and Lee's Analytical solution for Blast Waves

This section details a simplified formulation for the analytical blast wave solution proposed by Bach and Lee². The solution corresponds to unsteady 1-D blast waves propagating along the axis 'r'. We start off by defining non-dimensional parameters for the velocity (u), pressure (p) and density (ρ) fields.

$$\phi(\xi, \eta) = \frac{u(r, t)}{R_s(t)} \quad (6)$$

$$f(\xi, \eta) = \frac{p(r, t)}{\rho_0 R_s^2} \quad (7)$$

$$\psi(\xi, \eta) = \frac{\rho(r, t)}{\rho_0} \quad (8)$$

In the above equation, $\xi = \frac{r}{R_s(t)}$, $\eta = \frac{c_0^2}{R_s^2} = \frac{1}{M_s^2}$, ρ_0 is the density of the gas at far-field, R_s is the radius of the blast wave, c_0 is the speed of sound and M_s is the Mach number of the blast wave. Additionally, we define two other non-dimensional parameters, θ and y .

$$\theta(\eta) = \frac{R_s \dot{R}_s}{R_s^2} \quad (9)$$

$$y(\eta) = \left(\frac{R_s}{R_0}\right)^{j+1} \quad (10)$$

R_0 in Equation 10 is the characteristic explosion length, which quantifies the initial energy deposited to generate the blast wave. Writing down the mass (Equation 11), momentum (Equation 12), and energy (Equation 13) conservation assuming the flow field to be adiabatic and the gas to be perfect, we get,

$$(\phi - \xi) \left(\frac{\partial \psi}{\partial \xi}\right) + \psi \left(\frac{\partial \phi}{\partial \xi}\right) + j\phi \left(\frac{\psi}{\xi}\right) = 2\theta\eta \frac{\partial \psi}{\partial \eta} \quad (11)$$

$$(\phi - \xi) \left(\frac{\partial \phi}{\partial \xi}\right) + \theta\phi + \left(\frac{1}{\psi}\right) \frac{\partial f}{\partial \xi} = 2\theta\eta \frac{\partial \phi}{\partial \eta} \quad (12)$$

$$(\phi - \xi) \left(\frac{\partial f}{\partial \xi} - \frac{\gamma f}{\psi} \left(\frac{\partial \psi}{\partial \xi}\right)\right) + 2\theta f = 2\theta\eta \left(\frac{\partial f}{\partial \eta} - \frac{\gamma f}{\psi} \left(\frac{\partial \psi}{\partial \eta}\right)\right) \quad (13)$$

Conserving the total mass and total energy enclosed by the blast wave at any instant of time, we get the following mass and energy integrals,

$$\text{Mass Intergral: } \int_0^1 \psi \xi^j d\xi = \frac{1}{j+1} \quad (14)$$

$$\text{Energy Integral: } 1 = y \left(\frac{I}{\eta} - \frac{1}{\gamma(\gamma-1)(j+1)} \right), \text{ where } I = \int_0^1 \left(\frac{f}{\gamma-1} + \frac{\psi\phi^2}{2} \right) \xi^j d\xi \quad (15)$$

In the above equation, $j = 0, 1, 2$ for planar, cylindrical and spherical waves. The boundary conditions at the shock front ($\xi = 1$) can be obtained from standard normal shock relations.

$$\phi(1, \eta) = \left[\frac{2}{\gamma+1} \right] (1 - \eta) \quad (16)$$

$$f(1, \eta) = \left[\frac{2}{\gamma+1} \right] - \left[\frac{\gamma-1}{\gamma(\gamma+1)} \right] \eta \quad (17)$$

$$\psi(1, \eta) = \frac{\gamma+1}{\gamma-1+2\eta} \quad (18)$$

We then assume a power law profile for the density field behind the blast wave.

$$\psi(\xi, \eta) = \psi(\xi, \eta) \xi^{q(\eta)} \quad (19)$$

The exponent, $q(\eta)$, is determined by substituting Equation 19 into Equation 14 and solving for the mass integral. This yields the following equation for $q(\eta)$.

$$q(\eta) = (j + 1)[\psi(1, \eta) - 1] \quad (20)$$

Simplifying Equation 11 by substituting for the density profile from Equation 19, we get,

$$\frac{\partial \phi}{\partial \xi} + (q + j) \left(\frac{\phi}{\xi} \right) = q + \frac{2\theta\eta}{\psi(1, \eta)} [1 + (j + 1)\psi(1, \eta) \ln \xi] \left(\frac{d\psi(1, \eta)}{d\eta} \right) \quad (21)$$

Solving Equation 21, subject to the boundary condition that $\phi(0, \eta) = 0$, we can obtain an expression for the particle velocity profile.

$$\phi = \phi(1, \eta) \xi (1 - \Theta \ln \xi) \quad (22)$$

In the above equation,

$$\Theta = - \frac{2\theta\eta}{\phi(1, \eta) \psi(1, \eta)} \left(\frac{d\psi(1, \eta)}{d\eta} \right) \quad (23)$$

Substituting the density profile and particle velocity profile into Equation 12, we get the following expression for the pressure profile.

$$\begin{aligned} f(\xi, \eta) = & f(1, \eta) + f_2(\xi^{q+2} - 1) + f_3\{\xi^{q+2}[(q+2)\ln\xi - 1] + 1\} \\ & + f_4\{2 - \xi^{q+2}[(q+2)^2(\ln\xi)^2 - 2(q+2)\ln\xi + 2]\} \quad (24) \end{aligned}$$

In the above equation,

$$f_2 = \frac{\psi(1, \eta)}{q+2} \left[(1 - \Theta) \{ \phi(1, \eta) - \phi^2(1, \eta) \} - \theta \left\{ \phi(1, \eta) - 2\eta \left(\frac{d\phi(1, \eta)}{d\eta} \right) \right\} \right] \quad (25)$$

$$f_3 = \frac{\psi(1, \eta)}{(q+2)^2} \left(\theta \left\{ \Theta \phi(1, \eta) - 2\eta \left(\frac{d}{d\eta} [\Theta \phi(1, \eta)] \right) \right\} - \Theta \phi(1, \eta) - \Theta^2 \phi^2(1, \eta) + 2\Theta \phi^2(1, \eta) \right) \quad (26)$$

$$f_4 = \frac{\Theta^2 \phi^2(1, \eta) \psi(1, \eta)}{(q+3)^3} \quad (27)$$

We then evaluate the $\theta(\eta)$ by substituting for the velocity, density and pressure profiles in the energy equation (Equation 13).

$$\frac{d\theta}{d\eta} = - \frac{1}{2\eta} \left\{ \theta + 1 - 2\phi(1, \eta) - \frac{D_1 + 4\eta}{\gamma + 1} - (\gamma - 1)(j + 1) \left[\phi(1, \eta) - \frac{(D_1 + 4\eta)^2}{4\theta\gamma(\gamma + 1)} \right] \right\}$$

$$\begin{aligned}
& + \frac{D_1 + 4\eta}{8\eta^2(\gamma + 1)} \left[\frac{(D_1 + 4\eta)\phi(1, \eta)}{\theta} - \frac{\phi(1, \eta)(\gamma + 1)}{\theta\psi(1, \eta)} + 2(\eta + 1) + \frac{(\gamma - 1)(j + 1)(\gamma + 1)}{2\theta} \phi^2(1, \eta) \right] \\
& + \frac{2\theta[2 + (\gamma - 1)(j + 1)]}{D_1 + 4\eta} \quad (28)
\end{aligned}$$

Where, $D_1 = \gamma(j + 3) + (j - 1)$. In the above equation, the relation between y and η is unknown and can be obtained by differentiating Equation 10.

$$\frac{dy}{d\eta} = -(j + 1) \left(\frac{y}{2\theta\eta} \right) \quad (29)$$

To seek the solution of $\theta(\eta)$ and $y(\eta)$, these variables are expanded in a power series format and are solved numerically with the boundary condition at $\eta = 0$ ($\theta(0) = y(0) = 0$). Once the solutions of $\theta(\eta)$ and $y(\eta)$ are obtained, we can estimate the flow field profiles (velocity and pressure fields) using equations 22 and 24.

To determine the shock trajectory, we can integrate the expression, $\dot{R}_s = \frac{dR_s}{dt}$, to get the time evolution of R_s . This yields the following equation in terms of $\theta(\eta)$ and $y(\eta)$.

$$\frac{c_0 t}{R_0} = -\frac{1}{2} \int_0^\eta \frac{y^{j+1}}{\theta \sqrt{\eta}} d\eta \quad (30)$$

These plots comparing the solution (blast wave evolution) from the analytical formulation against experimental observations are presented in Supplementary Section S3.

S3. Calibrating the analytical blast wave solution for the current experimental configuration

The analytical blast wave model developed by Bach and Lee² requires an estimate of the characteristic explosion length (R_0), which characterises the energy deposited onto the copper wire for it to explode and generate a blast front of a characteristic strength. The value of R_0 corresponding to a specific blast strength can be obtained by iteratively fitting R_0 such that we obtain the desired value of the blast Mach number (M_s) at a desired location (R_s). In the current experiments, the blast wave Mach number at a distance of 264mm from the source of the explosion is known. This data is used to estimate R_0 using an iterative fitting routine.

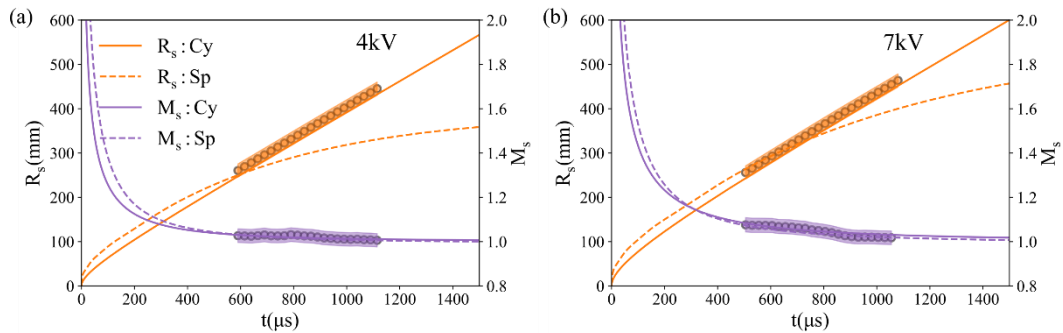


Figure S3. The plot compares the experimentally observed temporal evolution of the blast wave radius (R_s) and the blast wave Mach number (M_s) against the analytical blast wave model for cylindrical and spherical blast fronts. Panels (a) and (b) correspond to charging voltages of 4kV and 7kV, respectively. In the figure, the scatter plot with the error boundaries represents experimental data, while the solid lines correspond to the cylindrical blast solution and the dashed lines signify the spherical blast solution.

The theoretical blast wave model is then solved numerically to obtain the spatiotemporal evolution of the blast front, which is then compared against our experimental data. It is to be noted that the theoretical blast wave model is generalised for different geometries using a parameter, j , which assumes values of 0, 1 and 2 for planar, cylindrical and spherical blast fronts, respectively. As evident from Fig. S3, the experimental trends are found to align closely with cylindrical blast waves in comparison with spherical blast waves.

S4. Variation of v_{in} and Δp_{dip} across different values of $M_{s,r}$

Fig. S4 (a) plots the variation of Δp_{dip} (the difference between the ambient pressure and the lowest sub-ambient pressure imposed by the blast wave; marked in Fig. 4 of the manuscript) against $M_{s,r}$, alongside v_{in} . The plots reveal a monotonic rise in Δp_{dip} and v_{in} against $M_{s,r}$. When plotted on the log scale (Fig. S4 (b)), our experimental data reveals the following power-law correlation between Δp_{dip} and v_{in} .

$$\Delta p_{dip} \propto v_{in}^{0.15}$$

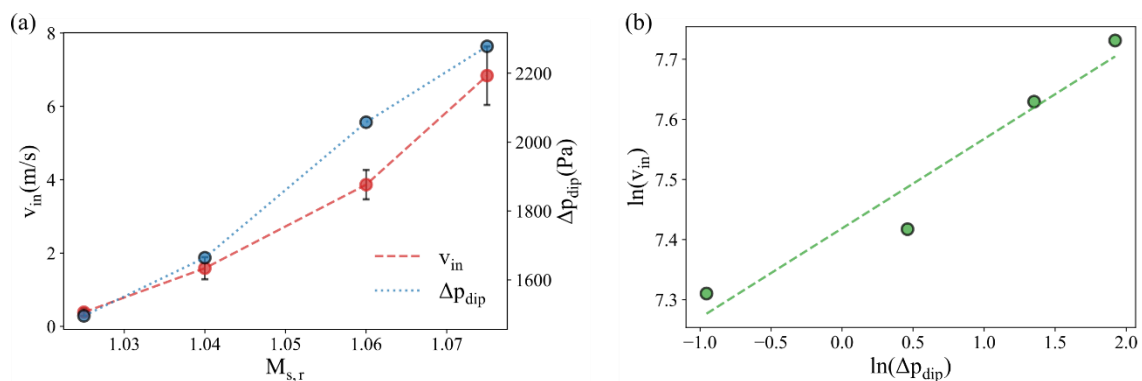


Fig. S4: (a) Plot depicting the variation of v_{in} and Δp_{dip} at different Mach numbers. (b) v_{in} and Δp_{dip} plotted on a log scale to illustrate their power law dependence.

S5. Schematic depicting the dynamics of Re-attachment and Extinction regimes

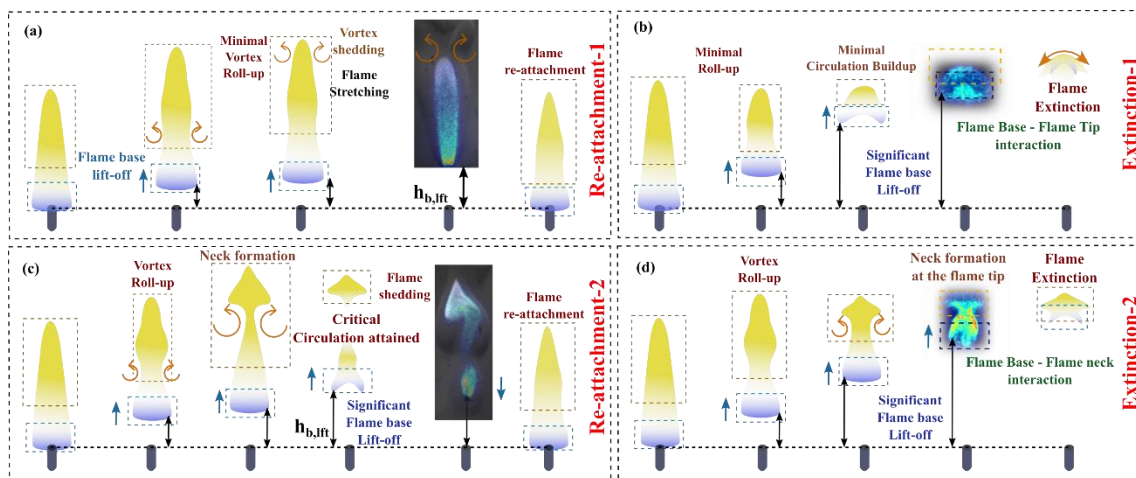


Fig. S5: (a, c) Schematics illustrating the Re-attachment Type-1 and Type-2 sub-regimes, respectively. (b, d) Schematics illustrating the Extinction Type-1 and Type-2 sub-regimes, respectively.

S6. Pressure gradient imposed by the blast wave at the flame base location

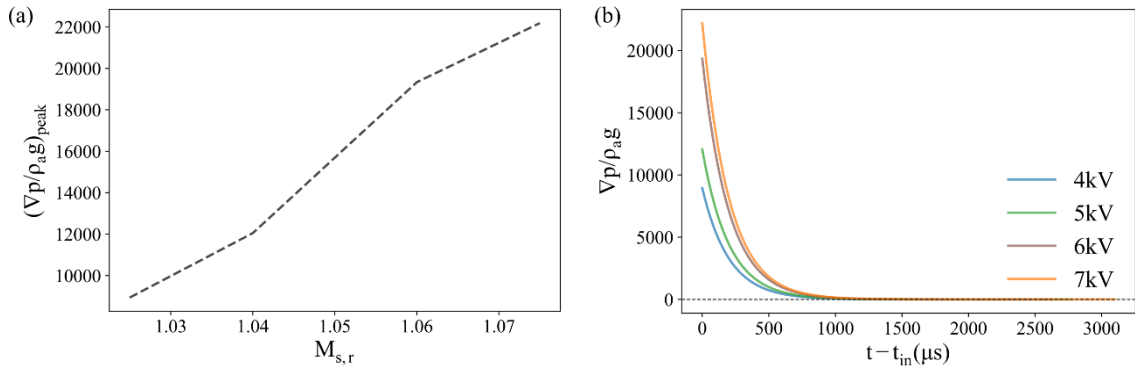


Fig. S6: (a) Variation of $\nabla p/(\rho_a g)$ against $M_{s,r}$. (b) Temporal variation of $\nabla p/(\rho_a g)$. Beyond a timescale of ~ 1 ms, the pressure gradient imposed by the blast drops to levels below the gravitational pressure gradient

S7. Formulation of the scaling law for $h_{b,lft}$ and $t_{b,lft}$

As the jet flame lifts off following the interaction with the induced flow, it develops an edge flame structure at its base. The structure forms as a result of the fuel (from the central jet) diffusing radially outward into the airstream and the entrainment of air into the central fuel jet (depicted in Fig. S7 (b)). This results in the formation of a fuel-air mixture fraction profile wherein we move from a fuel-rich zone to a fuel-lean zone as we move radially outward from the fuel jet axis. At the radial distance corresponding to the stoichiometric mixture fraction, a diffusion flame structure is established. Curved premixed flame branches encompass the diffusion front on the fuel-lean and fuel-rich side, resulting in the formation of an edge flame structure (depicted in Fig. S7 (b); right). Such flame structures in lifted non-premixed flames were explored in detail by Buckmaster et al³ and Vadlamudi et al⁴.

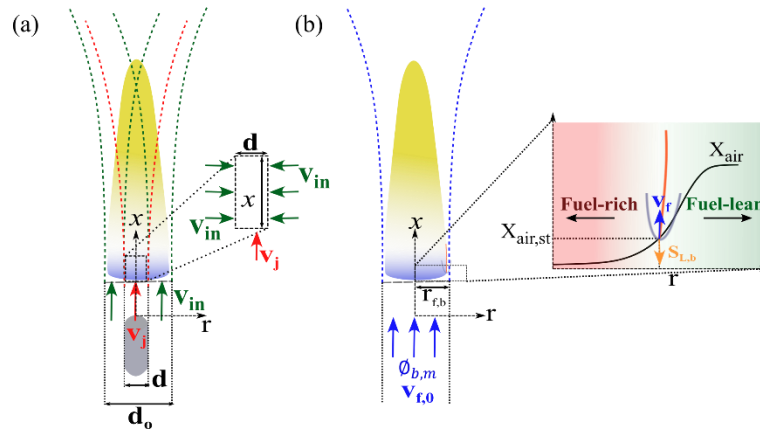


Fig. S7: (a) Schematic of the co-axial jet approximation. Entrainment of air into the fuel stream is depicted on the right. (b) Equivalent single jet with the combined momentum flux as the co-axial jets. The edge flame structure of the lifted flame is shown on the right, with the non-premixed front sketched in orange and the premixed branches in grey.

Owing to the edge flame structure developed at the flame base, the lifted jet flame can propagate upstream with a characteristic velocity, which can be a multiple of the laminar unstretched flame speed³. Thus, during the process of lift-off, the lift-off rate of the flame base (dx_b/dt), can be scaled as the difference between the effective convective velocity of the reactant stream into the flame base (v_f) and the effective upstream propagation velocity of the edge flame ($S_{L,b}$). This is expressed mathematically in Equation 31.

$$\left| \frac{dx_b}{dt} \right| \sim (v_f - S_{L,b}) \quad (31)$$

The above equation is valid for $(t_0 + t_{b,ra}) > t > t_0$ wherein the flame is in the lifted state. t_0 is the time instant at which the flame base lifts off, and $t_{b,ra}$ is the time taken for the flame base to reattach to the nozzle tip following lift-off. Both v_f and $S_{L,b}$ are dependent on the extent of mixing between the central fuel stream and the surrounding air stream.

Formulation of the scaling laws for $h_{b,lft}$ and $t_{b,lft}$

Following Equation 31, we see that, when the flame reaches its maximum lift-off height ($h_{b,lft}$) (i.e, when the term $\frac{dx_b}{dt}$ becomes zero), the convective velocity of the reactant stream into the edge flame is balanced out by its upstream flame propagation velocity.

$$v_f(r_{f,b}, h_{b,lft}) \sim S_{L,b}(r_{f,b}, h_{b,lft}) \quad (32)$$

In the above equation, $r_{f,b}$ is the radius of the flame base, and is depicted in Fig. S7 (b). The parameters $v_f(r_{f,b}, h_{b,lft})$ and $S_{L,b}(r_{f,b}, h_{b,lft})$ in Equation 32 can be modelled by approximating the induced flow as an impulsively started steady co-axial air flow around the jet flame during the period of flame lift-off (Fig. S7 (a)). The rationale behind the approach is that only a portion of the induced flow in the immediate vicinity of the fuel jet interacts with the jet flame. Consequently, the induced flow can be treated as a coaxial jet characterized by an outer diameter (d_o) and an inner diameter (d_i), surrounding the fuel jet, as depicted in Fig. S7 (a). The outer diameter (d_o) is further approximated to scale with the diameter of the flame base ($d_{f,b} = 2r_{f,b}$). The problem thus reduces to that of steady co-axial jets, where the inner jet transports fuel (of density ρ_j) with a velocity of v_j , while the outer jet delivers air (of density ρ_a) at a velocity of v_{in} .

Estimation of $v_f(r_{f,b}, h_{b,lft})$

We can now reduce the co-axial jet problem to that of an equivalent single open jet (with a velocity scale of $v_{f,0}$) that has the same momentum flux as the co-axial jets combined.

$$v_{f,0} = \sqrt{\left(\frac{\rho_j}{\rho_a}\right) \left(\frac{d}{d_o}\right)^2 v_j^2 + \left(\frac{d_o^2 - d^2}{d_o^2}\right) v_{in}^2} \quad (33)$$

Consequently, we can then estimate the velocity field of the equivalent single (open) jet by modelling it as a Schlichting jet⁵.

$$v_f(r, x) = \frac{256v}{3} \frac{Re_f}{\left(\frac{32}{3}\right)^2 \left(\frac{x}{Re_f}\right) + r \left(\frac{r Re_f}{x}\right)^3 + \frac{64r}{3} \left(\frac{r Re_f}{x}\right)} \quad (34)$$

In the above equation, Re_f is the Reynolds number of the equivalent single jet estimated based on $v_{f,0}$ and d_o . Corresponding to our experimental conditions, where $Re_f \gg 1$, Equation. 34, estimated at $x = h_{b,lft}$ and $r = r_{f,b}$ (corresponding to the edge flame location at the maximum flame base lift-off height) reduces to,

$$v_f(r_{f,b}, h_{b,lft}) \sim \frac{(v h_{b,lft})^3}{v_{f,0}^2 d^2 d_o^4} \quad (35)$$

Estimation of $S_{L,b}(r_{f,b}, h_{b,lft})$

The flame speed of the upstream propagating edge flame can be expressed as a multiple (denoted as A ; $\sim O(10^0)$) of the unstretched flame speed. The unstretched flame speed can be estimated using flame speed correlations, provided the effective equivalence ratio at the flame base is determined. To achieve

this, Villermaux's mixing model⁶ for coaxial jets is applied to estimate the mixing between the fuel and air streams. The model estimates the mass flux of air (outer jet) entrained into the inner fuel jet as $\rho_a v_{in}$ (Fig. S7 (a)). This entrainment alters the effective equivalence ratio at the flame base ($\phi_{b,m}$), which can now be calculated based on the mass fluxes of the air and fuel streams into a cylindrical control volume of height x enclosing the fuel stream (Fig. S7 (a)).

$$\phi_{b,m} = \left(\frac{\rho_j}{\rho_a}\right) \left(\frac{v_j}{v_{in}}\right) \left(\frac{d}{4x}\right) \left(\frac{1}{\chi_{st}}\right) \quad (36)$$

In the above equation, χ_{st} represents the stoichiometric fuel-to-air mass ratio for methane combustion and is a constant. It should be noted that Equation 36 only estimates the mean value of the equivalence ratio at an axial distance of x . To obtain the radial distribution of the equivalence ratio, we adopt the formulation of Vadlamudi et al.⁴, wherein a Gaussian profile is assumed for the normalised equivalence ratio ($\Phi = \frac{\phi}{\phi_{+1}}$) variation along the radial direction. The Gaussian profile is solved under the assumption that the air mass fraction at $r = 0$ (centre of the fuel jet) is zero. Additionally, the solution ensures that the mean value of the equivalence ratio equals the above estimated value of $\Phi_{b,m}$ ($= \frac{\phi_{b,m}}{1+\phi_{b,m}}$).

$$\Phi(r, x) = \exp\left(-\frac{r^2}{r_s^2(\Phi_{b,m}(x))}\right) \quad (37)$$

In the above equation, r_s is the length scale that quantifies the radial spread of the Gaussian profile, and scales with the length scale associated with mass diffusion during the period of flame base lift-off ($r_s \sim \sqrt{Dt_{b,lft}} \sim 10^{-3}m$; D is the binary diffusion coefficient of methane in air).

Equation. 37 is then evaluated at $x = h_{b,lft}$ and $r = r_{f,b}$, which corresponds to the location of the edge flame at the maximum flame base lift-off height.

$$\Phi(r_{f,b}, h_{b,lft}) = \exp\left(\frac{-r_{f,b}^2 \left[1 + \left(\frac{\rho_j}{\rho_a}\right) \left(\frac{v_j}{v_{in}}\right) \left(\frac{d}{4h_{b,lft}}\right) \left(\frac{1}{\chi_{st}}\right)\right]}{r_s^2 \left[\left(\frac{\rho_j}{\rho_a}\right) \left(\frac{v_j}{v_{in}}\right) \left(\frac{d}{4h_{b,lft}}\right) \left(\frac{1}{\chi_{st}}\right)\right]}\right) \quad (38)$$

The resulting normalised equivalence ratio (Equation 38) is then used in the flame speed – equivalence ratio correlation⁷, to estimate the value of the flame speed of the edge flame at that equivalence ratio (Equation 39).

$$S_{L,b}(r_{f,b}, h_{b,lft}) = 0.422A \left[\frac{\Phi(r_{f,b}, h_{b,lft})}{1-\Phi(r_{f,b}, h_{b,lft})}\right]^{0.15} \exp\left(-5.18 \left[\frac{\Phi(r_{f,b}, h_{b,lft})}{1-\Phi(r_{f,b}, h_{b,lft})} - 1.075\right]^2\right) \quad (39)$$

Estimation of $h_{b,lft}$ and $t_{b,lft}$

As stated earlier, at $x = h_{b,lft}$, $\frac{dx_b}{dt} = 0$, and $v_f(r_{f,b}, h_{b,lft}) \sim S_{L,b}(r_{f,b}, h_{b,lft})$. Thus, from Equations 35 and Equation 39, we get,

$$h_{b,lft}^3 \sim \frac{v_{f,0}^2 d^2 d_0^4}{v^3} 0.422A \left[\frac{\Phi(r_{f,b}, h_{b,lft})}{1-\Phi(r_{f,b}, h_{b,lft})}\right]^{0.15} \exp\left(-5.18 \left[\frac{\Phi(r_{f,b}, h_{b,lft})}{1-\Phi(r_{f,b}, h_{b,lft})} - 1.075\right]^2\right) \quad (40)$$

Evaluating the above equation in the limit of our experimental conditions, wherein $\frac{h_{b,lft}}{d} \sim (10^0 - 10^1)$, the term $0.422A \left[\frac{\Phi(r_{f,b}, h_{b,lft})}{1-\Phi(r_{f,b}, h_{b,lft})}\right]^{0.15} \exp\left(-5.18 \left[\frac{\Phi(r_{f,b}, h_{b,lft})}{1-\Phi(r_{f,b}, h_{b,lft})} - 1.075\right]^2\right)$ reduces to a near constant value (denoted as k) across all experimental conditions explored in the current work. This reduces Equation 40 to,

$$h_{b,lft} \sim \left(k \frac{d^2 d_0^4}{\nu^3} \right)^{1/3} v_{f,0}^{2/3} \Rightarrow \frac{h_{b,lft}}{d} \sim \left(\frac{k d_0^2}{\nu d} \right)^{1/3} Re_f^{2/3} \quad (41)$$

Following similar lines, an estimate for the timescale associated with flame base lift-off ($t_{b,lft}$) can be obtained as,

$$t_{b,lft} \sim \frac{h_{b,lft}}{v_f(r_{f,b}, h_{b,lft})} \quad (42)$$

Simplifying the above equation by substituting for $v_f(r_{f,b}, h_{b,lft})$ from Equation 35, we get,

$$\frac{t_{b,lft}}{t_{diff}} \sim \frac{1}{t_{diff}} \left(\frac{d^2 d_0^2}{k^2 \nu} \right)^{1/3} Re_f^{2/3} \quad (43)$$

In the above equation, t_{diff} is the characteristic diffusion time scale and is estimated as $t_{diff} = d^2/D$, and remains constant across the explored parametric space.

For a more detailed derivation, the readers are referred to the work of Aravind et al.⁸, wherein the correlations are developed in a general framework that is applicable for both premixed and non-premixed jet flames.

S8. Estimation of $d\bar{u}/dt$

$d\bar{u}/dt$ can be estimated using the momentum conservation equation as shown below,

$$\frac{d\bar{u}}{dt} = -\frac{\nabla p}{\rho} + \left(\frac{\rho - \rho_a}{\rho} \right) \bar{g} + \nu \nabla^2 \bar{u}$$

As explained in Section 3.1 of the manuscript, $\nabla p = 0$ in the above equation for quiescent conditions and in the presence of the induced flow. Neglecting viscous dissipation effects⁹, the above equation simplifies to,

$$\frac{d\bar{u}}{dt} = \left(\frac{\rho - \rho_a}{\rho} \right) \bar{g}$$

REFERENCES

1. Otsu, N. A Threshold Selection Method from Gray-Level Histograms. *IEEE Transactions on Systems, Man, and Cybernetics* **9**, 62–66 (1979).
2. BACH, G. G. & LEE, J. H. S. An analytical solution for blast waves. *AIAA Journal* **8**, 271–275 (1970).
3. Buckmaster, J. Edge-flames. *Progress in Energy and Combustion Science* **28**, 435–475 (2002).
4. Vadlamudi, G., Aravind, A. & Basu, S. Insights into the flame transitions and flame stabilization mechanisms in a freely falling burning droplet encountering a co-flow. *Journal of Fluid Mechanics* **977**, A29 (2023).

5. Schlichting, H. Laminare Strahlausbreitung. *Z. angew. Math. Mech.* **13**, 260–263 (1933).
6. Villermaux, E. & Rehab, H. Mixing in coaxial jets. *J. Fluid Mech.* **425**, 161–185 (2000).
7. Gülder, Ö. L. *Correlations of Laminar Combustion Data for Alternative S.I. Engine Fuels*.
<https://www.sae.org/publications/technical-papers/content/841000/> (1984) doi:10.4271/841000.
8. Aravind, A., Vadlamudi, G. & Basu, S. Response of premixed Jet Flames to Blast Waves. Preprint
at <https://doi.org/10.48550/arXiv.2312.04887> (2024).
9. Xia, X. & Zhang, P. A vortex-dynamical scaling theory for flickering buoyant diffusion flames. *J. Fluid Mech.* **855**, 1156–1169 (2018).